

# Fast measurements of concentration profiles inside deformable objects in microflows with reduced spatial coherence digital holography

Christophe Minetti,<sup>1,\*</sup> Natacha Callens,<sup>1</sup> Gwennou Coupier,<sup>2</sup>  
Thomas Podgorski,<sup>2</sup> and Frank Dubois<sup>1</sup>

<sup>1</sup>Microgravity Research Center, Université Libre de Bruxelles, 50 Avenue F. Roosevelt,  
CP 165/62, B-1050 Brussels, Belgium

<sup>2</sup>Laboratoire de Spectrométrie Physique, Université Joseph Fourier—Grenoble I, 140 Rue de la Physique,  
F-38402 St. Martin d'Hères Cedex, France

\*Corresponding author: cminetti@ulb.ac.be

Received 9 June 2008; revised 13 August 2008; accepted 3 September 2008;  
posted 8 September 2008 (Doc. ID 97163); published 7 October 2008

We investigate the use of a digital holographic microscope working with partially coherent spatial illumination to study concentration profiles inside confined deformable bodies flowing in microchannels. The studied phenomenon is rapidly changing in time and requires the recording of the complete holographic information for every frame. For this purpose, we implemented one of the classical methods of off-axis digital holography: the Fourier method. Digital holography allows one to numerically investigate a volume by refocusing the different planes of depth, allowing one to locate the objects under investigation in three dimensions. Furthermore, the phase is directly related to the refractive index, thus to the concentration inside the body. Based on simple symmetry assumptions, we present an original method for determining the concentration profiles inside deformable objects in microconfined flows. Details of the optical and numerical implementation, as well as exemplative experimental results are presented.

© 2008 Optical Society of America

OCIS codes: 090.0090, 100.0100, 180.0180, 070.0070, 090.1760.

## 1. Introduction

Optical microscopy is limited by the small depths of focus due to high numerical apertures of the microscope lenses and the high magnification ratios. The extension of the depth of focus is thus an important goal in optical microscopy. In this way, digital holography microscopy (DHM) yields the reconstruction in depth [1] and is very promising in optical microscopy because it considerably expands the field of investigation.

In DHM, holograms are recorded with a CCD camera and provide both phase and intensity maps. The complex amplitude can be computed to refocus the

depth images of a thick sample slice by slice (by implementing the Kirchhoff–Fresnel equation). In addition, the phase is the significant information used to quantitatively measure the optical path length of a sample, which is not available from measurements by classical optical methods [2]. DHM has been applied in numerous applications of interest, such as observation of biological samples [3–6], living cells culture analysis [7–9], and accurate measurements of refractive indices inside cells and even 3D tomography [10,11]. Optical scanning holography, an unconventional form of digital holography, has been used to explore 3D microscopy [12].

DHM is very flexible for implementing powerful holographic information processing techniques [13]. For example, methods to correct phase aberration [14–16], to perform 3D pattern recognition [17–19],

to process border artifacts [20], to emulate classical phase contrast imaging [6,9], to perform phase imaging [21], to implement autofocus algorithms [22,23], and to perform object segmentation [24] have been proposed.

In parallel, several optical methods have been implemented to extract the phase and amplitude information from the recorded interference pattern [1,25,26]. For dynamic phenomena, a crucial point is the acquisition time. Indeed, phase stepping methods need the acquisition of several images, which restricts the applications to objects slowly varying in time. Conversely, the Fourier method [27–29] is very suitable for fast phenomena because it requires only one recorded hologram in order to compute the complex amplitude.

In this paper, quantitative phase map analysis is proposed to study concentration profiles inside phospholipid vesicles in a microfluidic flow. Vesicles are lipid membranes enclosing an inner solution and suspended into an outer one. Vesicles can be considered as model systems to reproduce the mechanical properties of living cells, especially simple ones like red blood cells. For that reason, the study of their dynamics under flow is the object of increasing attention. When flowing in a straight channel whose width and thickness are of the same order as their diameter, vesicles adopt a stationary centered bullet-like or a parachutelike shape, resulting from the balance between the hydrodynamic stresses and the membrane elasticity [a typical example is shown in Fig. 2(a) below] [30,31]. These shapes are also observed for capsules, droplets, or blood cells. Beyond the description of this stationary shape of the membrane, and given the fact that membranes are permeable to water, one can wonder how this affects the flow field and solute concentration profiles inside and outside vesicles. Since the solutions are generally transparent aqueous solutions, phase contrast microscopy is a advantageous tool to investigate these properties.

The use of DHM provides the phase information and offers the refocusing capability useful for quantitatively studying, for every hologram, a complete volume, which is not possible with a classical phase contrast microscope [2,5,19]. From the phase map, one can easily derive the optical path length of the object and the refractive index difference linked to the concentrations inside and outside the body. However, owing to the integration along the optical axis, deriving concentration profiles from a single holographic image is not straightforward and requires the implementation of specific image processing techniques. We propose an original method for determining the concentration profiles by making simple symmetry assumptions on the studied bodies. By coupling an automatic best focus [22] determination with a phase map compensation and a segmentation process, we will present a way to derive concentration profiles inside a flowing vesicle confined in a microchannel. Integrated refractive index measure-

ment has been proposed previously for living cell applications [32–34].

Usually, DHM is implemented with a coherent laser beam. However, highly coherent sources are very sensitive to any defect in the optical path in such a way that the results can be badly corrupted by the coherent artifact noise. To reduce the effect of this noise and avoid multiple reflection interferences, we developed a DHM with a partial coherent illumination in a Mach–Zehnder configuration [5,35]. Because we are working with dynamic phenomena, it is mandatory to get the complete digital holographic information for every recorded image with a short exposure time. The illumination is performed by a laser diode, and the reduced spatial coherence is obtained by focusing the laser beam close to a rotating ground glass. It has been demonstrated that partial spatial illumination significantly increases the quality of the holographic images [35], in particular when the experimental cell, as it is the case for this paper, cannot be optimized with respect to the optical quality.

In Section 2, the optical setup is briefly described, and the technical specifications of the microscope are provided. Section 3 is devoted to the image processing techniques used to perform the determination of the concentration profile. These techniques are implemented on the exemplary case of flowing vesicles, according to an experimental setup that is described in Section 4. Results and discussion are presented in Section 5.

## 2. Optical Setup Description

This section describes the DHM setup used for our experimental investigation. The optical setup is described in Fig. 1. It is a Mach–Zehnder interferometer in a microscope configuration working with a

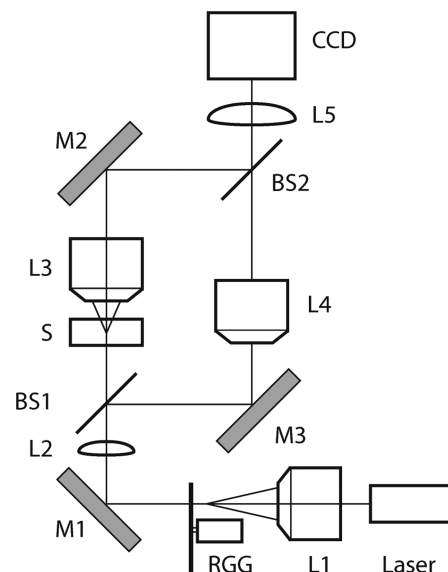


Fig. 1. Optical setup of the digital holographic microscope. L1, focusing lens; RGG, rotating ground glass for spatial coherence reduction; L2, collimating lens; L3, L4, identical microscope lenses ( $\times 20$ ); L5, refocusing lens; CCD, charge-coupled device camera; M1–M3, mirrors; BS1, BS2, beam splitters.

partial spatial coherent source. The spatial partial coherence is achieved by focusing a coherent beam (a monomode laser diode,  $\lambda = 635$  nm) with a lens (L1) close to a rotating ground glass (RGG). The spatial partial coherence of the source is adjusted by changing the position of the focused spot on the RGG plane [27]. The use of partial coherence reduces the coherent noise and provides a temporal-coherence-like effect that eliminates the coherent multiple reflection effect [35]. In our experiment, the setup has been adjusted to achieve a coherence length of about  $150\ \mu\text{m}$ .

The field of view of the DHM is  $524\ \mu\text{m} \times 420\ \mu\text{m}$ . The camera is a JAI CV-M4 camera with a CCD array of  $1280 \times 1024$  pixels (cropped in a  $1024 \times 1024$  pixel window to match the fast Fourier transform computation). The exposure time is set to  $200\ \mu\text{s}$ , allowing us to record flowing objects without blurring effect. The angle between the reference and the object beam is adjusted in such a way that a gratinglike thin interference pattern is recorded on the sensor. This results in a high-fringe-density hologram (one fringe corresponds to 6 pixels) that is used to implement the Fourier method to compute the complex amplitude of the object beam [28,29].

### 3. Description of Algorithms

In the general case, it is impossible to determine exactly the 3D distribution of the refractive index from the phase obtained with DHM without making additional assumptions [36]. To get a 3D map, one should use tomographic techniques, which require several images and are slow. Refractive index tomography has been successfully implemented in various applications [37–41]. However, in our case, by making symmetry assumptions for the objects under investigation, it is possible to determine the 2D refractive index map integrated along the optical axis and derive the mean value of the refractive index inside the objects. Note that with symmetry assumptions one could recreate the different views obtained by a tomograph and retrieve the 3D repartition of the refractive index inside the object with only one image obtained by digital holography. Nevertheless, because the phase is defined modulo  $2\pi$  and because the precise measurement of the refractive index difference inside a vesicle from the phase map is not straightforward, specific image processing techniques are required. This section describes the different algorithms developed to extract the optical path length in each point of the object from the recorded hologram. We start this section with a global overview of the processing sequence and follow with a more detailed description of the algorithms developed for the processing.

#### A. Overview Description

The developed sequence used can be described as follows: we consider one object (vesicle) flowing in a microchannel. Starting from the recorded hologram, we extract the amplitude and the phase and

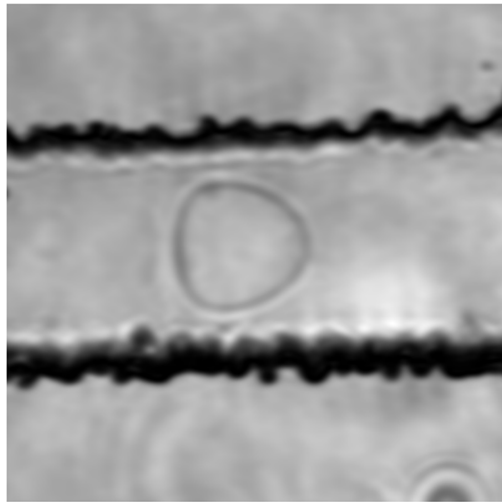
compute the complex amplitude  $U(x, y)$ , using the Fourier method. We crop a region of interest (ROI) around the approximate position  $(x_0, y_0)$  of the vesicle and seek the best focus position  $z_0$  of the object by reconstructing the cropped complex amplitude  $U'_d(x, y)$  slice by slice, where  $U'_d(x, y)$  is the cropped complex amplitude around  $(x_0, y_0)$  reconstructed at a distance  $d$  from the focus plane of the microscope. From this position,  $z_0$ , we compute the amplitude [and the intensity, Fig. 2(a)] and the phase map [Fig. 2(b)]. As the phase presents discontinuities (defined modulo  $2\pi$ ), we compute a compensated phase by removing the background phase. Then we perform a segmentation of the object to detect the boundaries of the body and derive the optical path length in each point of the body.

#### B. Best Focus Determination

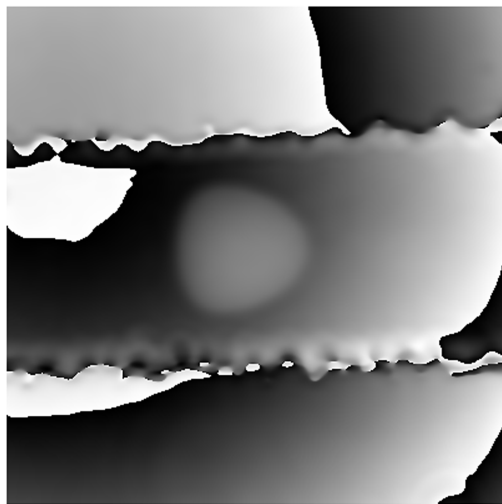
Digital holography allows one to numerically investigate a volume by refocusing the different slices but does not provide any information about the focus status. We have recently proposed a focus plane detection criterion by defining a new focus metric. This metric is the integral of the complex amplitude modulus. It has been shown [22] that this integral is maximum for pure phase objects when the reconstructed distance reaches the best focus plane. However, this criterion is based on an integral and gives a value that is influenced by all the objects distributed in the volume. In our application, the studied objects are confined in a microchannel whose walls interfere with the object when the best focus distance of the object is computed. For this reason, we perform local analysis by cropping the complex amplitude in a ROI around the object. We choose a ROI size very close to the object size (typically  $140 \times 140$  pixels) to avoid any unwanted contribution of the background or the walls of the channel, the ROI size always being smaller than the channel width. To avoid diffraction due to the borders of the hologram and that appears in digital holographic reconstruction, we extend the ROI size (typically to  $256 \times 256$  pixels) with values that minimize the borders diffraction [20]. By coupling those two methods (best focus and border extension), we automatically determine the best focus distance of the object. Because we are interested in the phase measurement, we first have to propagate the complex amplitude up to the best focus plane of the object before computing the phase map. Indeed, the digital propagation creates phase changes that distort the optical path length determination, leading to additional measurements errors in out-of-focus planes.

#### C. Phase Map Compensation

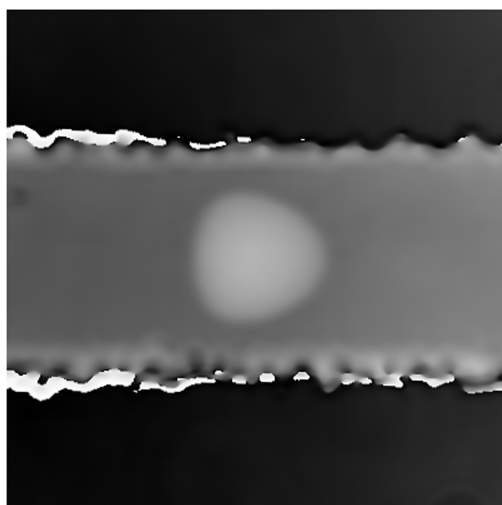
The phase map gives the optical path length integrated along the propagating axis of the illuminating wave, which is the basic information needed for this study (see Subsection 5.B). The phase map presents a nonuniform background phase owing to two sources of optical defects. First, the optical windows



(a)



(b)



(c)

Fig. 2. (a) Intensity image of a vesicle in a microchannel of  $80\ \mu\text{m}$  width. The vesicle is at a distance of  $19\ \mu\text{m}$  from the DHM focus plan. (b) Phase image of a vesicle in a microchannel. The phase values are remapped to 256 gray levels. (c) Compensated phase map of Fig. 2(b). The phase values are remapped to 256 gray levels.

of the experimental cell are not completely flat and are not exactly parallel to each other. Second, there is always a small misalignment of the interferometer. Therefore, it is necessary to implement a phase map correction. Because of the symmetry between the object and reference channels of the interferometer we are using, we implemented a fast method based on the phase map derivative. The complex amplitude  $U(x,y)$  is expressed by

$$U(x,y) = A(x,y) \exp[i\phi(x,y)]. \quad (1)$$

The measured phase  $\phi(x,y)$  is the sum of the phase induced by the object and the background phase that corresponds to the phase obtained when no object is present in the optical system:

$$\exp[i\phi(x,y)] = \exp[i\beta(x,y)] \exp[i\phi(x,y)], \quad (2)$$

where  $\beta(x,y)$  is the background phase and  $\phi(x,y)$  is the object phase that we want to measure. This phase addition results in global phase differences (over the field of view) larger than  $2\pi$ , introducing jumps in the phase map that complicate the refractive index variations from the measured phase. To solve this problem, one usually unwraps the phase before converting it to refractive index data. Several methods have been proposed to solve the complex problem of phase unwrapping [42]. However, those methods require heavy computations that can be limiting to process large amount of data. Furthermore, phase unwrapping does not compensate for aberrations and is therefore not a good way to measure the phase delay introduced by the object. In our application, the measured refractive index difference between the object and the surrounding solution is sufficiently small to avoid phase jumps bigger than  $2\pi$  when the phase map is adequately corrected. Therefore, we use a compensation method to remove the background phase  $\beta(x,y)$ . Because of the symmetry of the interferometer, we assume that the background phase  $\beta(x,y)$  is modeled by a quadratic phase expressed by

$$\beta(x,y) = \sigma_x(x - x_0)^2 + \sigma_y(y - y_0)^2, \quad (3)$$

where  $(x_0, y_0)$  are the coordinates of the center of the parabola and  $\sigma_x$  and  $\sigma_y$  are the curvatures along the  $x$  and  $y$  axes. Note that a similar modeling of the phase map by a polynomial function has been successfully proposed and implemented [43] for phase compensation aberration. As outlined above, the phase change induced by the objects is relatively small. One can thus assume that the measured phase  $\phi(x,y)$  is relatively close to the background phase  $\beta(x,y)$  and can be determined by fitting  $\phi(x,y)$  by Eq. (3). However, this fitting cannot be computed directly from  $\phi(x,y)$  owing to phase jumps. To remove those discontinuities, the fitting is performed on the derivative of the phase map [44]. The parameters  $x_0$ ,  $y_0$ ,  $\sigma_x$ , and  $\sigma_y$  of the quadratic phase factor result from a least

mean squares method by minimizing the following expression:

$$\begin{aligned} \psi(\sigma, x_0, y_0) = & \sum_{x=1}^N \sum_{y=1}^N \left| \left[ \frac{\delta}{\delta x} \left( \exp\{i\varphi(x, y)\} \right. \right. \right. \\ & \times \left. \left. \exp\{i[\sigma_x(x - x_0)^2 + \sigma_y(y - y_0)^2]\} \right) \right] \right|^2 \\ & + \left| \left[ \frac{\delta}{\delta y} \left( \exp\{i\varphi(x, y)\} \exp\{i[\sigma_x(x - x_0)^2 \right. \right. \right. \\ & \left. \left. \left. + \sigma_y(y - y_0)^2]\} \right) \right] \right|^2, \end{aligned} \quad (4)$$

which gives the values of  $\sigma_x$ ,  $\sigma_y$ ,  $x_0$ , and  $y_0$  and determines  $\beta(x, y)$ .

The difference in the refractive index of the fluid and the microchannel walls introduces strong phase variations between the zone of interest and the rest of the field of view. For this reason, the compensation defined by Eq. (3) is computed only on the phase values inside the microchannel. The compensated phase is then subtracted from the measured phase as follows:

$$\begin{aligned} \phi(x, y) &= \varphi(x, y) - \beta(x, y) \quad \text{if } \varphi(x, y) > \beta(x, y), \\ \phi(x, y) &= 2\pi - \varphi(x, y) + \beta(x, y) \quad \text{if } \varphi(x, y) < \beta(x, y), \end{aligned} \quad (5)$$

which results in a phase map  $\phi(x, y)$  with a homogeneous background inside the channel and a smooth bright shape representing the optical path length of the studied object. A typical example of phase map compensation is shown in Fig. 2(c). The optical path length of the body is then obtained by comparing the value of the phase in each point inside the body with those outside the microchannel. This is true under the assumption that the compensated phase is perfect. In practice, the reference phase may not be exactly quadratic and is obtained through a fitting procedure. Nevertheless, around the object under study (in the ROI), we can consider the remaining compensated phase to be linear, and it can be approximated by a plane with a specific orientation. To avoid a tilting effect, we remove this background phase by computing the plane fitting the border of the ROI around the object. This provides a ROI with the object surrounded by a constant background. To get the optical path length of the object, we now have to extract the object from its surrounding background.

#### D. Segmentation

The segmentation process aims at delimiting the boundaries of the object under study and gets rid of the noisy small values of the optical path length just around the edges of the vesicle (inherent to the Fourier method). The simplest way is to apply a threshold computed on the basis of the mean value of the background. This is convenient for objects with sharp edges but not sufficiently precise for vesicles

whose boundaries are very smooth. We will see in Subsection 5.B that our symmetry assumptions require a fine determination of the body shape. Furthermore, the Fourier method used to extract the phase has a blurring effect on the object due to the low-pass filtering. Active contour techniques are iterative processes that attempt to minimize a defined function and are much more suitable for application with smooth boundaries. Starting from an initial contour centered on the object, the successive iterations deform the contour until the function is minimized and the deformed contour fits the boundaries of the object. We used an active contour algorithm based on the Mumford–Shah functional minimization [45]. Our motivation for choosing the active contour technique is guided by the following: we know the position  $(x_0, y_0)$  of the object and its approximate shape, around which we have cropped the ROI. Thus, as an initial contour we can reasonably choose a circle with a ray equal to 2/3 of the size of the ROI. From the contour, we extract the matrix  $\Phi(x, y)$  corresponding to the phase in each point of the object and having null values outside the object. The error on the segmentation of the borders of the objects is estimated to be about 2% of the object width. This error is estimated by comparing the segmented shape obtained on ten different vesicles (of different sizes) to their width and height obtained manually.

The optical path length  $e(x, y)$  of the body is then defined by

$$e(x, y) = \frac{\Phi(x, y)\lambda}{2\pi}, \quad (6)$$

where  $\lambda$  is the wavelength of the illumination source (635 nm).

#### 4. Objectives and Experimental Description

The techniques described in the previous sections are applied on vesicles under flow. The core of the experimental device consists in a straight channel made by soft lithography in a polydimethylsiloxane (PDMS) piece glued to a glass slide. Except for a few dust particles in the PDMS, the whole system is homogeneous and transparent. Vesicles are prepared following the electroformation method [46]. They are made of a dioleoylphosphatidylcholine (DOPC) lipid bilayer enclosing an internal solution of sucrose in water. Samples are diluted in a slightly hyperosmotic external solution of glucose. In the following, we consider a  $80 \mu\text{m} \times 80 \mu\text{m}$  channel of square cross section in which the Poiseuille flow is controlled by applying a pressure difference between the inlet and outlet. The flow rate varies from around  $3 \times 10^{-4}$  to  $10^{-2} \mu\text{l/s}$ . Vesicles flowing in this microchannel have a length between 20 and  $40 \mu\text{m}$  and a width between 10 and  $30 \mu\text{m}$ . To measure how they are deflated relative to a sphere, they are characterized by their reduced volume  $\nu \leq 1$  defined by  $\nu = V/V_0$ , where  $V$  is the volume of the vesicle

and  $V_0$  is the volume of the sphere of same surface as the considered vesicle. The typical reduced volumes are in the range  $0.9 \leq \nu \leq 1$ . According to the flow rate, the vesicles flow at a velocity varying from 100 to 4000  $\mu\text{m/s}$ .

The results presented in the next section have been widely observed for vesicles whose size, reduced volume, and velocity lie in the ranges presented above. As demonstrative examples, we focus on two typical vesicles, whose characteristics are summarized in Table 1.

## 5. Results

### A. Specific Processing

Images are recorded at a frame rate of 24 frames/s with an exposure time of 200  $\mu\text{s}$ . On every recorded hologram, the complex amplitude (intensity and phase) is computed and the processing sequence described in Section 3 is applied (best focus determination, phase compensation, and segmentation). The ROI, centered on the vesicle, is given by hand; further processing steps are performed automatically to obtain, for each occurrence of the object, the matrix  $h(x, y)$  corresponding to the thickness of the object at each point and null values outside the object. We observed that, only a few micrometers away from the vesicle, the phase in the external solution is not influenced by the passage of the vesicle; therefore we can consider the refractive index  $n_1$  of the external solution to be constant, and the resulting background phase can be approximated by a quadratic phase map.

### B. Experimental Demonstration

For every frame, we can consider the optical path length  $e$  of the vesicle given by Eq. (6), which is also defined by

$$e(x, y) = 2h(x, y)\Delta n(x, y). \quad (7)$$

$2h(x, y)$  is its real thickness, while  $\Delta n(x, y) = n_2(x, y) - n_1$  is the refractive index difference between the internal and the external solutions and  $n_2(x, y)$  is the mean value along the  $z$  axis of the local index  $n_2(x, y, z)$ .

In the most general case, one has to deal with two unknown functions of  $x$  and  $y$ , namely,  $h(x, y)$  and  $\Delta n(x, y)$ , of which only the product is known. Therefore, to determine them, one needs additional assumptions or information to extract relevant data from Eq. (7).

An important simplification of the problem is obtained when one considers a straight channel with a square cross section. In this case, when the vesicle

is centered in the channel, its transverse cross sections can be assumed to be as thick as wide for symmetry reasons.

For each cross section defined by its  $x_i$  along the longitudinal axis, one can thus consider the profile  $e(x_i, y)/2$ . Two such profiles for vesicle 1 are shown in Fig. 3. For every value of  $x_i$ , the path length profile is well fitted by half an ellipse:  $e(x_i, y)/2 = \alpha(x_i)[R(x_i)^2 - y^2]^{1/2}$ .

In particular, the square shape of the channel cross section has no footprint on the vesicle shape. This was expected, since the flow in the central part is quasi axisymmetric [47] and the elasticity of the membrane also tends to favor an axisymmetric shape. Then, we can consider that the profile  $h(x_i, y)$  is a half-circle,  $h(x_i, y) = [R(x_i)^2 - y^2]^{1/2}$ , and therefore that the scaling factor  $\alpha(x_i)$  is equal to  $\Delta n(x_i, y)$ , which is then  $y$  independent.

The variations of  $\Delta n(x)$  as a function of  $x$  are shown in Fig. 4 for vesicle 1 for three different velocities (189, 916, and 4006  $\mu\text{m/s}$ ). Each curve is obtained by averaging over ten different positions in the channel to decrease the noise, whose importance will be discussed later.

One can clearly observe a gradient from back to front inside the vesicle, which increases with the flow rate. To our knowledge, this is the first experimental observation of this phenomenon, which was not predicted theoretically. The uncertainties inherent to the method should therefore be discussed. We first focus on those specific to the nonoptical part (that is, the channel) in order to evaluate those associated with the optical setup.

A first source of error is associated with the uncertainties in the determination of the width and thickness of the channel. The latter was determined by measuring the thickness of the channel mold with a profilometer, of precision  $\pm 100$  nm. Within this error, the thickness was found to be constant all along the channel.

As one can see in Fig. 2, the edges of the channel are not totally straight because of the quality of the lithography mask. This leads to uncertainties in the width of  $\pm 3$   $\mu\text{m}$ . This could introduce a variation of around 5% of the scaling factor of the cross section. Under the (unrealistic) assumption that the vesicle completely reproduces this deviation from the symmetry, this leads to a maximum error of 5% in the determination of  $\Delta n$ .

Second, the measurement can be altered by some inhomogeneities in the field of view, such as dust trapped in the PDMS or floating around the vesicle. This alteration can be estimated by comparing measurements made at different positions in the

Table 1. Characteristics of the Vesicles Presented for Demonstration

	Inner Solution	Outer Solution	Size	Reduced Volume
Vesicle 1	300 mM sucrose	350 mM glucose	24 $\mu\text{m} \times 30 \mu\text{m}$	0.96
Vesicle 2	300 mM sucrose	370 mM glucose	32 $\mu\text{m} \times 40 \mu\text{m}$	0.99

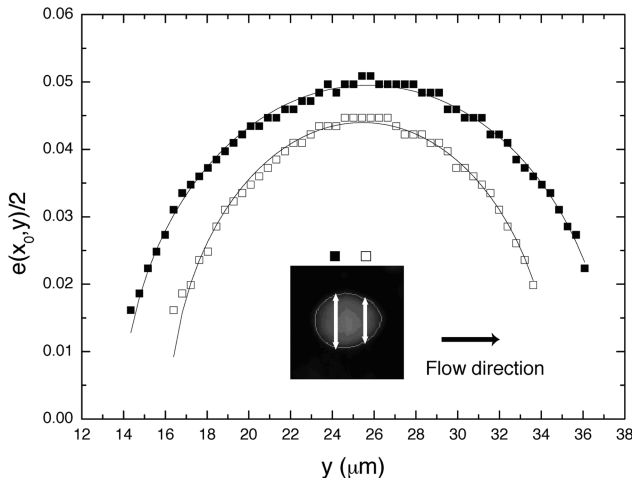


Fig. 3. Half optical width  $e(x_0, y)/2$  along two cross sections located at two different positions  $x_0$  along the longitudinal axis of vesicle 1. Inset, location of these cross sections on the compensated phase image of the vesicle. Solid curves show the fits with a half-ellipse.

channel. The related error (standard deviation in this set of measures) has been estimated to less than 10%. This error drops to a minimum value of 1% when averaging is performed over a few dozen frames. This value, which can be estimated by considering two equivalent passages of the vesicle, can be considered the one associated with the optical device. Note that this is also the error associated with the pixelization of the signal in the  $Oxy$  plane; no other source of error has been identified.

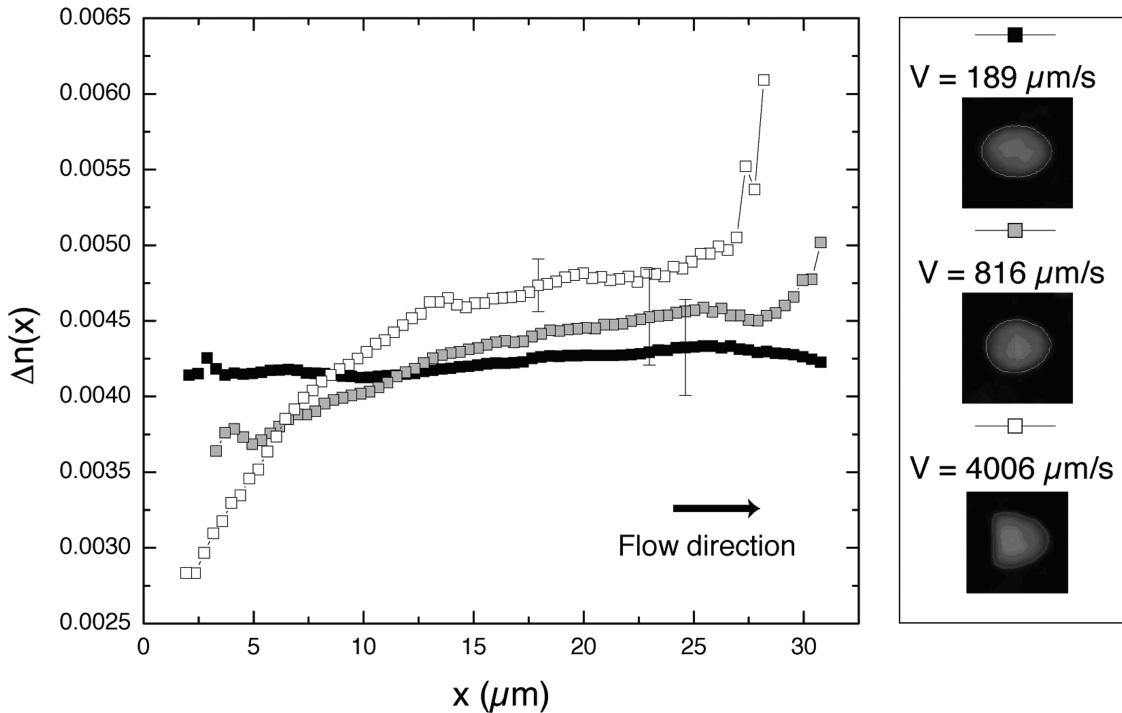


Fig. 4. Evolution of the index  $\Delta n(x)$  along the longitudinal axis of the vesicle for three different vesicle velocities (average over ten measurements for each velocity, to get rid of the local inhomogeneities of the channel: for clarity, only one typical error bar is shown on each curve).  $x = 0$  corresponds to the rear of the vesicle, which is moving from left to right. The right-hand part of the figure shows the corresponding shapes given by the compensated phase image.

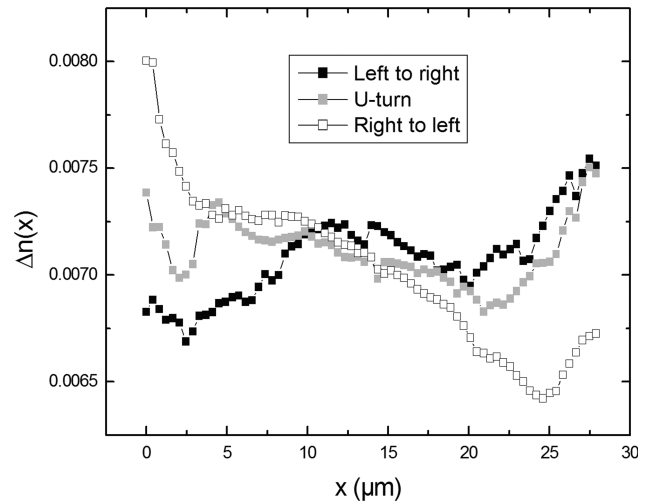


Fig. 5. Index gradient inside vesicle 2 doing a U-turn. The time step between two curves is  $1/24$  s. During the  $1/12$  s corresponding to the three curves shown, the vesicle has just reversed its fore-aft shape but has only moved a few micrometers. Nevertheless, the gradient inversion is clear. Note that each curve corresponds to a single frame, and is thus noisier than the curves of Fig. 4.

Consequently, the variations of  $\Delta n$  with  $x$  and the flow rate can be trusted. This gradient is directly linked with a gradient in the sugar concentration  $C_2$ . The corresponding variations are of a few millimolar concentrations [48], to be compared with the mean value  $\langle C_2 \rangle$ , which is around 300 mM. Note that it would be practically impossible to measure such

tiny variations of concentrations by techniques such as light absorption or fluorescence intensity.

The existence of such gradients around a vesicle while the concentration in the carrier fluid is homogeneous has never been reported in the literature. Since the vesicle's membrane is permeable to water but not to big molecules such as sugar, the flow through this membrane is induced by both osmotic and hydrodynamic pressure. The hydrodynamic pressure, which could be a motor for gradient creation through sugar advection, is generally much lower than the osmotic pressure difference induced by as little as a 1 mM concentration difference across the membrane. It is thus generally considered that osmotic pressure is the leading contribution and thus tends to homogenize the concentration profiles. However, these considerations are generally based on a quasi-static view of the problem, in which case the notion of osmotic pressure is well defined. In this situation, membrane permeability measurements can be easily carried out, for instance, by sucking a part of a vesicle into a micropipette. The permeabilities associated with the hydrodynamic and osmotic pressure were shown to be roughly of the same order [49,50]. However, Nardi *et al.*, who studied the osmotic-pressure-induced movement of a vesicle placed in an externally imposed concentration gradient, showed that a model based on such a quasi-static view yields a drift velocity more than 3 orders of magnitude lower than the measured one [51]. To our knowledge, no theoretical model is available in the literature to explain this. As noticed by Nardi *et al.*, in their experiments—as in ours—the vesicle is placed in a dynamic situation for which the notion of osmotic pressure is not well defined, or at least cannot be as well decoupled from the hydrodynamic pressure as in the quasi-static case. Moreover, the membrane permeabilities can be modified by the flow stress and may vary locally, since they depend on the membrane tension [49], which is not uniform along the flowing vesicle [52].

The understanding of how the solute species are distributed around a moving vesicle is thus still an open problem. Qualitatively, the existence of a gradient can be understood through general considerations. The key feature in the fact that the vesicle speed is lower than the flow speed in the middle of the channel [30]: the vesicle is only partly pushed by the flow, while a water stream still goes through it. Therefore, inside the vesicle, sugar must be advected to the front, leading to a concentration gradient inside the vesicle. Simultaneously, due to water permeation through the membrane, glucose concentration inhomogeneities build up in a boundary layer outside the vesicle. This leads to another gradient near the membrane. The final result is given by the sum of both gradients, whose relative weight is controlled by the permeation laws across the membrane, which to date are not known in such a dynamic case. Note that our analysis takes into account the possible existence of a boundary layer

outside the vesicle. This layer must be thin, since no modification of the phase is observed a few micrometers away from the vesicle. Thus the axisymmetry assumptions that were made for a vesicle remain valid for the vesicle and its surrounding layer.

It is also interesting to take advantage of the fast acquisition time of the DHM to explore transient states. An example is given in Fig. 5, where we show the gradients inside vesicle 2 doing a U-turn because of a flow reversal. We can see that the gradient inversion is very fast and is well measured by our technique.

## 6. Concluding Remarks

This paper describes a technique to measure concentration profiles inside deformable transparent bodies (vesicles) in microconfined flows at high frame rate. We used a digital holographic microscope working with a spatial partially coherent source created by focusing a laser diode beam close to a rotating ground glass. The use of partial coherence strongly reduces the inherent coherent noise generated by the optical defects of the experimental cell (microchannel) that is not of high optical quality. By coupling the phase information provided by interferometry and the refocusing capability of digital holography, we can derive the optical path length of vesicles everywhere in the channel depth at a high frame rate (24 frames/s). To cope with the vesicle velocities in the channel, we implemented the Fourier method.

Several algorithmic methods have been coupled to extract, from the recorded hologram, the thickness matrix of the vesicle. We first seek the best focus plane by using a specific criterion. The compensation of the phase map allows us to avoid discontinuities due to the periodicity of the phase map. Finally, the segmentation extracts the vesicle from its background. By making simple physical symmetry assumptions, we simplify the problem of precisely measuring the refractive index difference between the internal and the external solution. It has been shown that our method makes it possible to measure in a very reproducible way concentration profiles inside the flowing vesicle with a very good resolution. Note that these profiles are measured *in situ* with no specific preparation of the solutions, and the method could be applied to bodies such as red blood cells without taking the risk to modify their properties. This technique also opens new perspectives for the measurement of time-varying concentrations at microscopic scales in objects moving in an unsteady flow.

The authors acknowledge financial support from the European Space Agency (ESA) and Centre National d'Etudes Spatiales (CNES). This work was supported by the SSTC/ESA-PRODEX (Services Scientifiques Techniques et Culturels/European Space Agency-Programmes de Développement d'expériences) contract 90171.

## References

1. T. Zhang and I. Yamaguchi, "Three-dimensional microscopy with phase-shifting digital holography," *Opt. Lett.* **23**, 1221–1223 (1998).
2. E. Cucho, F. Bevilacqua, and C. Depeursinge, "Digital holography for quantitative phase contrast imaging," *Opt. Lett.* **24**, 291–293 (1999).
3. T. Ikeda, G. Popescu, R. R. Dasari, and M. S. Feld, "Hilbert phase microscopy for investigating fast dynamics in transparent systems," *Opt. Lett.* **30**, 1165–1167 (2005).
4. G. Popescu, T. Ikeda, C. A. Best, K. Badizadegan, R. R. Dasari, and M. S. Feld, "Erythrocyte structure and dynamics quantified by Hilbert phase microscopy," *J. Biomed. Opt.* **10**, 060503 (2005).
5. F. Dubois, L. Joannes, and J.-C. Legros, "Improved three-dimensional imaging with digital holography microscope using a partial spatial coherent source," *Appl. Opt.* **38**, 7085–7094 (1999).
6. F. Dubois, C. Yourassowsky, and O. Monnom, "Microscopie en holographie digitale avec une source partiellement cohérente," in *Imagerie et Photonique pour les Sciences du Vivant et la Médecine*, M. Faupel, P. Smigielski, and R. Grzymala, eds. (Fontis Média & Formatis, 2004), pp. 287–302.
7. P. Marquet, B. Rappaz, P. J. Magistretti, E. Cucho, Y. Emery, T. Colomb, and C. Depeursinge, "Digital holographic microscopy: a noninvasive contrast imaging technique allowing quantitative visualization of living cells with subwavelength axial accuracy," *Opt. Lett.* **30**, 468–470 (2005).
8. D. Carl, B. Kemper, G. Wernicke, and G. von Bally, "Parameter-optimized digital holographic microscope for high-resolution living-cell analysis," *Appl. Opt.* **43**, 6536–6544 (2004).
9. F. Dubois, C. Yourassowsky, O. Monnom, J.-C. Legros, O. Debeir, P. Van Ham, R. Kiss, and C. Decaestecker, "Digital holographic microscopy for the three-dimensional dynamic analysis of *in vitro* cancer cell migration," *J. Biomed. Opt.* **11**, 054032 (2006).
10. N. Lue, G. Popescu, T. Ikeda, R. R. Dasari, K. Badizadegan, and M. S. Feld, "Live cell refractometry using microfluidic devices," *Opt. Lett.* **31**, 2759–2761 (2006).
11. F. Charrière, A. Marian, F. Montfort, J. Kühn, T. Colomb, E. Cucho, P. Marquet, and C. Depeursinge, "Cell refractive index tomography by digital holographic microscopy," *Opt. Lett.* **31**, 178–180 (2006).
12. T.-C. Poon, K. Doh, B. Schilling, M. Wu, K. Shinoda, and Y. Suzuki, "Three-dimensional microscopy by optical scanning holography," *Opt. Eng.* **34**, pp. 1338–1344 (1995).
13. T.-C. Poon, ed., *Digital Holography and Three-Dimensional Display: Principles and Applications* (Springer, 2006).
14. P. Ferraro, S. De Nicola, A. Finizio, G. Coppola, S. Grilli, C. Magro, and G. Pierattini, "Compensation of the inherent wave front curvature in digital holographic coherent microscopy for quantitative phase-contrast imaging," *Appl. Opt.* **42**, 1938–1946 (2003).
15. T. Colomb, J. Kühn, F. Charrière, C. Depeursinge, P. Marquet, and N. Aspert, "Total aberrations compensation in digital holographic microscopy with a reference conjugated hologram," *Opt. Express* **14**, 4300–4306 (2006).
16. L. Miccio, D. Alfieri, S. Grilli, P. Ferraro, A. Finizio, L. De Petrocellis, and S. De Nicola, "Direct full compensation of the aberrations in quantitative phase microscopy of thin objects by a single digital hologram," *Appl. Phys. Lett.* **90**, 041104 (2007).
17. T.-C. Poon and T. Kim, "Optical image recognition of three-dimensional objects," *Appl. Opt.* **38**, 370–381 (1999).
18. D. Kim and B. Javidi, "Distortion-tolerant 3-D object recognition by using single exposure on-axis digital holography," *Opt. Express* **12**, 5539–5548 (2004).
19. F. Dubois, C. Minetti, O. Monnom, C. Yourassowsky, and J.-C. Legros, "Pattern recognition with digital holographic microscope working in partially coherent illumination," *Appl. Opt.* **41**, 4108–4119 (2002).
20. F. Dubois, O. Monnom, C. Yourassowsky, and J.-C. Legros, "Border processing in digital holography by extension of the digital hologram and reduction of the higher spatial frequencies," *Appl. Opt.* **41**, 2621–2626 (2002).
21. G. Indebetouw, Y. Tada, and J. Leacock, "Quantitative phase imaging with scanning holographic microscopy: an experimental assessment," *BioMed. Eng. OnLine* **5**, 63 (2006).
22. F. Dubois, C. Schockaert, N. Callens, and C. Yourassowsky, "Focus plane detection criteria in digital holography microscopy by amplitude analysis," *Opt. Express* **14**, 5895–5908 (2006).
23. W. Li, N. C. Loomis, Q. Hu, and C. S. Davis, "Focus detection from digital in-line holograms based on spectral  $l_1$  norms," *J. Opt. Soc. Am. A* **24**, 3054–3062 (2007).
24. C. P. McElhinney, J. B. McDonald, A. Castro, Y. Frauel, B. Javidi, and T. J. Naughton, "Depth-independent segmentation of macroscopic three-dimensional objects encoded in single perspectives of digital holograms," *Opt. Lett.* **32**, 1229–1231 (2007).
25. I. Yamaguchi and T. Zhang, "Phase-shifting digital holography," *Opt. Lett.* **22**, 1268–1270 (1997).
26. M. Sebesta and M. Gustafsson, "Object characterization with refractometric digital Fourier holography," *Opt. Lett.* **30**, 471–473 (2005).
27. F. Dubois, N. Callens, C. Yourassowsky, M. Hoyos, P. Kurowsky, and O. Monnom, "Digital holographic microscopy with reduced spatial coherence for three-dimensional particle flows analysis," *Appl. Opt.* **45**, 864–871 (2006).
28. T. Kreis, "Digital holographic interference-phase measurement using the Fourier-transform method," *J. Opt. Soc. Am. A* **3**, 847–855 (1986).
29. M. Takeda, H. Ina, and S. Kobayashi, "Fourier-transform method of fringe-pattern analysis for computer-based topography and interferometry," *J. Opt. Soc. Am.* **72**, 156–160 (1982).
30. V. Vitkova, M. Mader, and T. Podgorski, "Deformation of vesicles flowing through a capillary," *Europhys. Lett.* **68**, 398–404 (2004).
31. H. Noguchi and G. Gompper, "Shape transitions of fluid vesicles and red blood cells in capillary flows," *Proc. Natl. Acad. Sci. USA* **102**, 14159–14164 (2005).
32. B. Kemper, S. Kosmeier, P. Langehanenberg, G. von Bally, I. Bredebusch, W. Domschke, and J. Schnekenburger, "Integral refractive index determination of living suspension cells by multifocus digital holographic phase contrast microscopy," *J. Biomed. Opt.* **12**, 054009 (2007).
33. B. Rappaz, P. Marquet, E. Cucho, Y. Emery, C. Depeursinge, and P. J. Magistretti, "Measurement of the integral refractive index and dynamic cell morphometry of living cells with digital holographic microscopy," *Opt. Express* **13**, 9361–9373 (2005).
34. B. Rappaz, F. Charrière, C. Depeursinge, P. J. Magistretti, and P. Marquet, "Simultaneous cell morphometry and refractive index measurement with dual-wavelength digital holographic microscopy and dye-enhanced dispersion of perfusion medium," *Opt. Lett.* **33**, 744–746 (2008).
35. F. Dubois, M.-L. Novella Requena, C. Minetti, O. Monnom, and E. Istasse, "Partial coherence effects in digital holographic microscopy with a laser source," *Appl. Opt.* **43**, 1131–1139 (2004).
36. S. S. Kou and C. J. R. Sheppard, "Imaging in digital holographic microscopy," *Opt. Express* **15**, 13640–13648 (2007).
37. N. M. Dragomir and X. M. G. A. Roberts, "Three-dimensional refractive index reconstruction with quantitative phase tomography," *Microsc. Res. Tech.* **71**, 5–10 (2008).

38. M. Debailleul, B. Simon, V. Georges, O. Haeberlé, and V. Lauer, "Holographic microscopy and diffractive microtomography of transparent samples," *Meas. Sci. Technol.* **19**, 074009 (8 pages) (2008).
39. W. Choi, C. Fang-Yen, K. Badizadegan, R. R. Dasari, and M. S. Feld, "Extended depth of focus in tomographic phase microscopy using a propagation algorithm," *Opt. Lett.* **33**, 171–173 (2008).
40. W. Choi, C. Fang-Yen, K. Badizadegan, S. Oh, N. Lue, R. R. Dasari, and M. S. Feld, "Tomographic phase microscopy," *Nat. Meth.* **4**, 717–719 (2007).
41. F. Charrière, N. Pavillon, T. Colomb, T. Heger, E. Mitchell, P. Marquet, B. Rappaz, and C. Depeursinge, "Living specimen tomography by digital holographic microscopy: morphometry of testate amoeba," *Opt. Express* **14**, 7005–7013 (2006).
42. D. C. Ghiglia and M. D. Pritt, *Two-Dimensional Phase Unwrapping. Theory, Algorithms, and Software* (Wiley-Interscience 1998).
43. T. Colomb, F. Montfort, J. Kühn, N. Aspert, E. Cucho, A. Marian, F. Charrière, S. Bourquin, P. Marquet, and C. Depeursinge, "Numerical parametric lens for shifting, magnification and complete aberration compensation in digital holographic microscopy," *J. Opt. Soc. Am. A* **23**, 3177–3190 (2006).
44. P. Ferraro, D. Alferi, S. D. Nicola, L. D. Petrocellis, A. Finizio, and G. Pierattini, "Quantitative phase-contrast microscopy by a lateral shear approach to digital holographic image reconstruction," *Opt. Lett.* **31**, 1405–1407 (2006).
45. D. Mumford and J. Shah, "Optimal approximation by piecewise smooth functions and associated variational problems," *Commun. Pure Appl. Math.* **42**, 577–685 (1989).
46. M. I. Angelova, S. Soleau, P. Meleard, J.-F. Faucon, and P. Bothorel, "Preparation of giant vesicles by external ac electric fields. Kinetics and applications," *Prog. Colloid Polym. Sci.* **89**, 127 (1992).
47. F. M. White, *Viscous Fluid Flow* (McGraw-Hill, 1974).
48. D. R. Lide, *Handbook of Chemistry and Physics* (CRC Press, 2008).
49. V. Vitkova, J. Genova, and I. Bivas, "Permeability and the hidden area of lipid bilayers," *Eur. Biophys. J.* **33**, 706–714 (2004).
50. K. Olbrich, W. Rawicz, D. Needham, and E. Evans, "Water permeability and mechanical strength of polyunsaturated lipid bilayers," *Biophys. J.* **79**, 321–327 (2000).
51. J. Nardi, R. Bruinsma, and E. Sackmann, "Vesicles as osmotic motors," *Phys. Rev. Lett.* **82**, 5168–5171 (1999).
52. R. Bruinsma, "Rheology and shape transitions of vesicles under capillary flow," *Physica A* **234**, 249–270 (1996).